Predictive Flux Control-Based Efficiency Optimization Strategy for Three-Level Inverter-Fed Linear Induction Machine Adapted to Linear Metro

Yirong Tang, *Graduate Student Member, IEEE*, Wei Xu, *Fellow, IEEE*, Jian Ge, *Member, IEEE*, Yongdao Shangguan, Yaohua Li, *Member, IEEE*, and Wenye Yuan

***Abstract*—The linear induction machine (LIM) in linear metro suffers from poor efficiency due to the large air gap, end effects, and long-term light load operating conditions. Although such issue has been improved by some LIM efficiency optimization strategies (EOSs), poor performance, and high harmonic loss caused by low switching frequency of large-capacity inverters have not been well addressed. To further improve the efficiency of LIM system under low switching frequency, this article proposes one predictive flux control-based EOS for three-level inverter-fed LIM system. First, one novel primary flux-based LIM loss model is built, with which the optimal primary flux for minimum loss can be derived analytically. Then, considering multiple control demands, a computationally efficient predictive control is proposed to manipulate optimal flux under low switching frequency. Through control targets conversion, sequential optimization and online adaptive adjustment, tuning work for all weighting factors is avoided. Finally, comprehensive experimental comparisons with the mature control strategy and the existing EOS in linear metro are investigated on one 3 kW arc induction machine. It is confirmed that more loss reduction and efficiency improvement for LIM can be effectively achieved with the proposed method under low switching frequency.**

***Index Terms*—Efficiency optimization strategy (EOS), linear induction machine (LIM), low switching frequency, predictive control, three-level neutral-point clamped (3L-NPC) inverter.**

Manuscript received 29 December 2023; revised 20 March 2024 and 2 June 2024; accepted 5 July 2024. Date of publication 11 July 2024; date of current version 4 September 2024. This work was supported in part by the National Natural Science Foundation of China under Grant 52277050, in part by the High-level Talent Program at Chinese Academy of Sciences under Grant 2Q2024000076, in part by the Shenzhen International Collaboration Project under Grant GJHZ20210705142539007, in part by Shenzhen Fundamental Research Project (General Program) under Grant JCYJ20230807143701003, and in part by the Fundamental Research Funds for the Central Universities under Grant YCJJ20242205. Recommended for publication by Associate Editor G. Konstantinou. *(Corresponding author: Wei Xu.)*

Yirong Tang, Jian Ge, and Yongdao Shangguan are with the State Key Laboratory of Advanced Electromagnetic Technology, School of Electrical and Electronic Engineering, Huazhong University of Science and Technology, Wuhan 430074, China (e-mail: yirtang@hust.edu.cn; gejian1994@hust.edu.cn; sgyd@hust.edu.cn).

Wei Xu and Yaohua Li are with the Key Laboratory of High Density Electromagnetic Power and Systems (Chinese Academy of Sciences), Institute of Electrical Engineering, Chinese Academy of Sciences, Beijing 100190, China, and also with the University of Chinese Academy of Sciences, Beijing 101408, China (e-mail: weixu@mail.iee.ac.cn; yhli@mail.iee.ac.cn).

Wenye Yuan is with the Zhuzhou CRRC Times Electric Company, Ltd., Zhuzhou 412001, China (e-mail: yuanwy@csrzic.com).

Color versions of one or more figures in this article are available at https://doi.org/10.1109/TPEL.2024.3425829.

Digital Object Identifier 10.1109/TPEL.2024.3425829

I. Introduction

DUE to the fast-growing population and limited resources of land in modern cities, urban transit is developing faster than ever in recent years. Compared to the rotary induction machine (RIM) traction systems, the linear induction machine (LIM) can get the direct thrust without transmission, and hence, enjoys stronger climbing capability, higher accelerations and decelerations, smaller turning radius, and so on [1], [2]. Due to these merits, the LIM drive systems have been developed and commercialized in more than 20 linear metro lines in the world, such as Kennedy airline in USA and Guangzhou Subway Lines 4–6 in China [3].

Meanwhile, with the continuous improvement of operating speed, newly built lines in urban transit mostly use 1500 V dc power supply mode to meet the requirements of high-power traction machines. Compared to two-level inverter, multilevel inverters-most prominently three-level neutral-point clamped (3L-NPC) inverter, have become a more attractive choice for high-power medium-voltage applications owing to its lower stress on semiconductor switches, lower switching frequency and less harmonic content [4]. Thereof, 3L-NPC inverter-fed LIM drives have broad technical advantages and application prospects in urban transit.

However, the cut-open of primary iron core in LIM leads to the dynamic end effects, resulting in the attenuation of air-gap flux and thrust. As a result, the equivalent magnetizing inductance is attenuated greatly and the equivalent secondary resistance increases rapidly [5]. Coupled with the influence of large air gap, the mechanical characteristics of LIM become softer. Under the same load, once the slip and the proportion of secondary slip loss increase, the working efficiency would get smaller quickly [6]. In addition, the LIM control strategies in linear metro are mostly based on slip frequency control or field oriented control (FOC), in which a constant excitation is used below the rated speed. However, the LIM in linear metro runs under light loads for a long time [7], i.e., cruising condition, which causes a huge copper loss with the constant excitation and further makes the working efficiency far lower than the rated efficiency.

To improve the LIM efficiency, some efficiency optimization strategies (EOSs), also known as loss minimization control, have been proposed most recently. They can be divided into two major categories, i.e., search controller-based strategies [8] and loss

model-based strategies [9], [10], [11]. The former iteratively searches for the optimal solution in order to find the minimum input power. The latter aims to establish a loss model based on the mathematical model, and derive an optimal solution with minimum loss. Although the search controller-based strategies can totally avoid the influence of parameters, model-based strategies are still the most studied and adopted EOSs currently due to the fast convergence, low thrust fluctuation, and strong stability.

However, in the existing methods, the optimal solution manipulation is realized on the framework of FOC with space vector modulation. In urban transit where the switching frequency is only controlled within hundreds of hertz, the harmonic content, and harmonic loss of FOC increase quickly due to the low carrier ratio modulation [12]. Meanwhile, the dynamic response and disturbance rejection ability also deteriorate under a long control period. Coupled with the complexity of inverter topology and model discretization, the existing FOC-based EOSs do not suit the high-power 3L-NPC inverter-fed LIM drives for efficiency improvement.

In opposition to FOC, predictive control uses the inverter states as manipulated variables directly, removes the modulator, and switches the inverter state only when needed, thus effectively reducing the switching frequency while maintaining control performance [13]. Thereof, predictive control is suggested as an alternative control scheme for high-power applications. Due to the increased number of discrete voltage vectors (VVs) and additional control requirements, such as neutral point voltage (NPV) balance, the control complexity is significantly increased when the predictive control is applied to 3L-NPC inverter. Thus, most researches in this topic are focused on reducing the algorithm complexity, such as a predefined switching table [14] or sector distribution methods [15], [16]. As for constraints such as switching frequency and NPV balance, they are generally introduced in the cost function by weighting factors [14], [17]. In this way, tuning work of the weighting factors are inevitably required. More importantly, it is difficult to solve the reference VV with multiple different dimensional goals, so that the optimal VV has to be selected through the cumbersome cost function enumeration.

Moreover, the primary flux magnitude, which is treated as another degree of freedom in predictive thrust and flux control branched methods, can be utilized to manipulate losses while maintaining fast and smooth thrust production. In [18] and [19], one primary flux based predictive control is presented, in which the flux reference derived from the maximum thrust per ampere (MTPA) is used to minimize the copper loss. In [20] and [21], the EOS is proposed for RIM by manipulating the stator flux with predictive flux control, in which two different stator flux-based loss models are derived. Moreover, Xie et al. [22] combined MTPA and EOS to effectively reduce loss in the whole speed range, while switching actions are penalized in cost function to reduce inverter loss. In [23], the efficiency optimization is achieved for field modulation motors by incorporating the harmonic-based loss minimization into predictive control. Existing investigations above prove that predictive flux control can provide an elegant solution for loss reduction without compromising dynamic performance. However, above methods

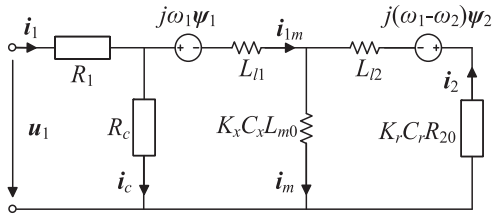

Fig. 1. Equivalent circuit of LIM in synchronous coordinate considering core loss.

are all adapted to two-level inverter, computational burden will become a crucial issue limiting its application in 3L-NPC inverter. Additionally, existing LIM loss models [10], [11] show high order and complex form. In order to match the predictive flux control scheme, further derivations with necessary simplifications are inevitable to obtain the analytical expression of optimal primary flux. These simplifications also affect the accuracy of optimal flux, thereby deteriorating the optimal point and efficiency optimization performance.

From the aforementioned, when implementing efficiency optimization for 3L-NPC inverter-fed LIM drive system under the framework of predictive flux control, at least the following three issues need to be properly addressed. First, an accurate and applicable primary flux-based LIM loss model needs to be constructed to obtain the optimal primary flux directly. Second, considering multiple additional demands in drive system, such as NPV balance and smooth switching transition, the computationally efficient predictive flux control under low switching frequency is urgently required. Third, with different dimensional control targets (flux and thrust tracking error, switching frequency, and NPV balance), tedious tuning work for multiple weighting factors should be well addressed.

To solve the above issues and realize LIM efficiency improvement under low switching frequency, this article proposes one predictive flux control-based efficiency optimization strategy (PFC-EOS) for 3L-NPC inverter-fed LIM drive system. Compared with the preliminary conference version [24], a more concise and applicable loss model is further derived, while the core-loss resistance and switching frequency constraint are fully considered in the implementation of PFC-EOS. Comprehensive experimental comparisons and analysis have been conducted, showing that better efficiency improvement can be effectively achieved for LIM under low switching frequency. Main contributions and advantages can be summarized as follows.

1) A novel primary flux-based loss model with full consideration of end effects is established. Compared to the existing LIM loss model [10], the proposed loss model has lower order and simpler optimal flux solution by adopting the primary field orientation.
2) Considering multiple control demands in drive system, a computationally efficient predictive control is proposed to manipulate flux under low switching frequency. By using the developed VV search method, the number of evaluations is reduced from 27 to at most 4 VVs.
3) Through control targets conversion, sequential optimization, and adaptive adjustment, tedious tuning work for

all weighting factors is avoided. In this way, design and implementation of PFC-EOS are greatly improved.

4) By manipulating the primary flux with the proposed PFC-EOS, the LIM efficiency under low switching frequency can be effectively improved over a wide speed and load range compared with the mature method in urban transit, PFC-MTPA [18], and FOC-EOS [10].

II. Model of LIM and 3L-NPC Inverter

A. Equivalent Circuit and Mathematical Model of LIM

Fig. 1 shows an equivalent circuit of LIM considering the core-loss resistance in the synchronous coordinate, where four coefficients are introduced to evaluate the influence of end effects on parameters [5], [25]. Based on the equivalent circuit, the model of LIM in the synchronous reference frame can be described as

$$\begin{cases} \boldsymbol{u}_1 = R_1\boldsymbol{i}_1 + p\boldsymbol{\psi}_1 + j\omega_1\boldsymbol{\psi}_1 \\ \boldsymbol{0} = R_{2eq}\boldsymbol{i}_2 + p\boldsymbol{\psi}_2 + j\left(\omega_1 - \omega_2\right)\boldsymbol{\psi}_2 \\ \boldsymbol{\psi}_1 = L_1\boldsymbol{i}_{1m} + L_{meq}\boldsymbol{i}_2 \\ \boldsymbol{\psi}_2 = L_{meq}\boldsymbol{i}_{1m} + L_2\boldsymbol{i}_2 \end{cases} \tag{1}$$

where $\boldsymbol{u}$, $\boldsymbol{i}$ and ψ are the voltage, current, and flux vectors, subscripts 1 and 2 stand for the primary and secondary parameters, R and L represent the resistance and inductance, ω_1 and ω_2 are the secondary flux angular velocity and secondary angular velocity, respectively. $\boldsymbol{i}_{1m} = \boldsymbol{i}_1 - \boldsymbol{i}_c$ is the flowing current through primary leakage, $\boldsymbol{i}_c$ the flowing current through core-loss branch, and p the differential operator. $L_{meq} = K_xC_xL_{m0}$ and $R_{2eq} = K_rC_rR_{20}$ are the equivalent magnetizing inductance and secondary resistance considering the end effects, where L_{m0} and R_{20} are the parameters when LIM is standstill, i.e., neglecting the end effects. The *Kr,x* and *Cr,x* mean the longitudinal end effect and transversal end effect coefficients, respectively, which reflect the influence of end effects on magnetizing inductance and secondary resistance. Detailed derivations and the definition of each coefficient can be found in [25].

The voltage and current in the core-loss branch are given by

$$\begin{cases} R_c\boldsymbol{i}_c = p\boldsymbol{\psi}_1 + j\omega_1\boldsymbol{\psi}_1 \\ \boldsymbol{i}_c = \boldsymbol{i}_1 + \boldsymbol{i}_2 - \boldsymbol{i}_m \end{cases} \tag{2}$$

where $\boldsymbol{i}_m$ is the magnetizing current and R_c the core-loss resistance.

And the output thrust of LIM can be expressed as

$$F_e = \frac{3\pi}{2\tau}\left[\psi_{1d}(i_{1q} - i_{cq}) - \psi_{1q}(i_{1d} - i_{cd})\right] \tag{3}$$

where τ is the pole pitch of the LIM.

B. Topology and Model of 3L-NPC Inverter

The topology of 3L-NPC inverter is shown in Fig. 2(a). With different switching states, each phase can be connected to either the positive (P), negative (N), or neutral (O) point of the dc-link. The space distribution of all the 27 discrete VVs produced by the 3L-NPC inverter in the $\alpha\beta$ plane is shown in Fig. 2(b), which can be categorized into four groups: large VVs $\{\boldsymbol{u}_1, \boldsymbol{u}_3, \ldots\boldsymbol{u}_{11}\}$,

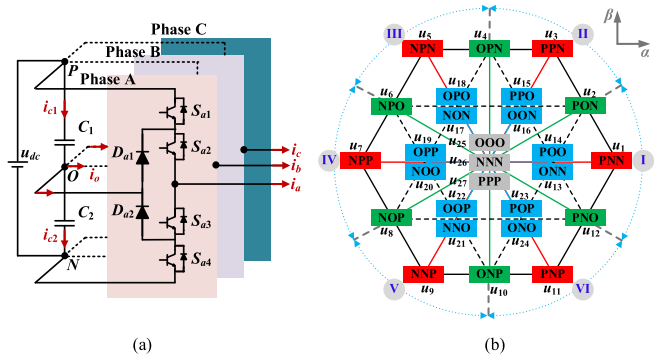

Fig. 2. 3L-NPC inverter and space vector. (a) Circuit topology. (b) Space distribution of all the admissible VVs.

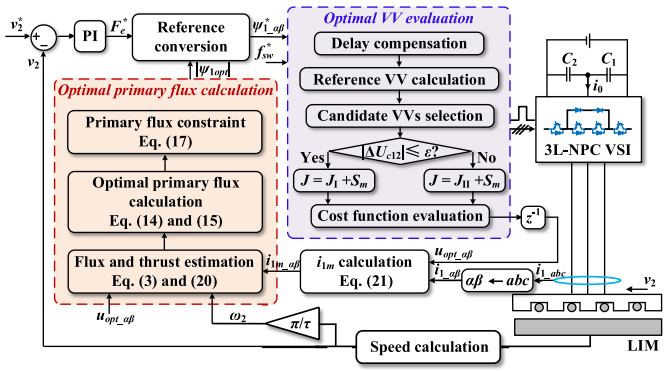

Fig. 3. Control block diagram of the proposed PFC-EOS for LIM drives.

medium VVs $\{\boldsymbol{u}_2, \boldsymbol{u}_4, \ldots\boldsymbol{u}_{12}\}$, small VVs $\{\boldsymbol{u}_{13}, \boldsymbol{u}_{14}, \ldots\boldsymbol{u}_{24}\}$, and zero VVs $\{\boldsymbol{u}_{25}, \boldsymbol{u}_{26}, \boldsymbol{u}_{27}\}$.

Compared to the two-level inverter, the NPV balance is one inherent requirement due to the topology of the 3L-NPC inverter. Hence, it is necessary to consider the NPV for both safe operation and satisfactory performance, as defined as

$$\Delta U_{c12} = U_{\mathrm{dc1}} - U_{\mathrm{dc2}} \tag{4}$$

where U_{dc1} and U_{dc2} are dc-link bus top and bottom capacitor voltages, respectively. Based on the Kirchhoff's current law and circuit topology, as shown in Fig. 2(a), the NPV at $(k+1)$th instant can be predicted, as given by

$$\Delta U_{c12}^{k+1} = \Delta U_{c12}^{k} + \frac{T_s}{C}\left(\left|S_a^k\right| i_a^k + \left|S_b^k\right| i_b^k + \left|S_c^k\right| i_c^k\right) \tag{5}$$

where $S_x\,(x = a, b, c)$ is the switching state of each phase and the superscript k denotes the variables at kth instant. In this article, S_x are labeled as "1," "0," and "-1" for the states P, O, and N, respectively. $C = C_1 = C_2$ represent the upper and lower dc-link capacitors. And T_s is the sampling period.

III. Proposed Predictive Flux Control-Based Efficiency Optimization Strategy

The overall control diagram of the proposed method is shown in Fig. 3, which is mainly composed of the following two parts: 1) optimal primary flux calculation and 2) manipulation. By

manipulating the primary flux reference, the predictive thrust and flux control branched methods provide an effective solution for loss reduction without compromising dynamic performance, especially under low switching frequency. To obtain the desired primary flux reference, a primary flux-based loss model is built firstly. Then, the flux manipulation method under low switching frequency for 3L-NPC inverter-fed LIM drives is given. The details are elaborated in the following.

A. Proposed Loss Model and Optimal Primary Flux of LIM

The total controllable loss of LIM, including core loss, primary and secondary copper losses, can be attained as

$$P_{\mathrm{LIM}} = \frac{3}{2} \left[R_1\left(i_{1d}^2 + i_{1q}^2\right) + R_{2eq}\left(i_{2d}^2 + i_{2q}^2\right) + R_c\left(i_{cd}^2 + i_{cq}^2\right)\right]. \quad (6)$$

It is noticeable that, since the LIM in linear metro is generally designed with relatively low average flux density, the magnetic saturation can be effectively avoided and, thus, is not included in this work. To model the LIM loss with the thrust and primary flux, the relationship between primary flux and current should be derived. First, considering the primary field orientation, i.e., $\psi_{1d} = |\psi_1|$ and $\psi_{1q} = 0$, it can be easily derived from (2) that $i_{cd} = 0$ and $i_{cq} = \omega_1 \psi_{1d}/R_c$ in steady state.

Second, the primary current can be modeled in terms of the primary flux as follows. The secondary voltage equation in (1) can be rewritten as

$$\mathbf{0} = R_{2eq}\boldsymbol{i}_2 + j(\omega_1 - \omega_2)\left(L_{meq}\boldsymbol{i}_{1m} + L_2\boldsymbol{i}_2\right). \quad (7)$$

Based on (7), the flowing current through primary leakage is further explained by the secondary current as follow:

$$\boldsymbol{i}_{1m} = -\frac{\boldsymbol{i}_2(R_{2eq} + j\omega_s L_2)}{j\omega_s L_{meq}} \quad (8)$$

where $\omega_s = \omega_1 - \omega_2$ is the slip angular velocity. By substituting (8) into the third term of (1), the orthogonal components of primary flux can be expressed by secondary current and slip angular velocity, as derived as

$$\begin{cases} \psi_{1d} = -\frac{R_{2eq}L_1}{L_{meq}}\left(\frac{\sigma L_2}{R_{2eq}} i_{2d} + \frac{1}{\omega_s} i_{2q}\right) \\ \psi_{1q} = -\frac{R_{2eq}L_1}{L_{meq}}\left(\frac{\sigma L_2}{R_{2eq}} i_{2q} - \frac{1}{\omega_s} i_{2d}\right) \end{cases} \quad (9)$$

where $\sigma = 1\text{-}L_{meq}^2/(L_1 L_2)$ is the leakage coefficient. On the basis of primary field orientation, it obtains $\sigma L_2 i_{2q}/R_{2eq} = i_{2d}/\omega_s$. In this way, the d-axis component of primary flux in (9) can be further simplified as

$$\psi_{1d} = -\frac{R_{2eq}L_1\omega_s}{L_{meq}}\left[\left(\frac{\sigma L_2}{R_{2eq}}\right)^2 + \frac{1}{\omega_s^2}\right] i_{2q} \approx -\frac{R_{2eq}L_1}{L_{meq}\omega_s} i_{2q}. \quad (10)$$

In (10), an approximation $(\sigma L_2/R_{2eq})^2 \ll 1/\omega_s^2$ is made. This approximation is valid since that the slip angular frequency is very small, and the difference between the two terms is further enlarged after squared. Therefore, ignoring $(\sigma L_2/R_{2eq})^2$ does not introduce a large error. For a given speed and load, the primary current in (6) can be obtained as functions of the primary flux according to (1)–(3) and (10), as written by

$$\begin{cases} i_{1d} = \frac{\psi_{1d}}{L_1} + \frac{4\tau^2\sigma L_1^2 L_2 {F_e}^2}{9\pi^2 L_{meq}^2 \psi_{1d}^3} \\ i_{1q} = \frac{2\tau F_e}{3\pi\psi_{1d}} + \frac{(\omega_2+\omega_s)\psi_{1d}}{R_c} \\ \omega_s = \frac{2\tau R_{2eq} L_1^2 F_e}{3\pi L_{meq}^2 \psi_{1d}^2}. \end{cases} \quad (11)$$

As for the secondary current, the relationship between the secondary slip loss and the output power can be established, as given by

$$P_{out} = F_e \times \frac{\omega_2 \tau}{\pi} = \frac{3}{2} R_{2eq}\left(i_{2d}^2 + i_{2q}^2\right)\frac{\omega_2}{\omega_s}. \quad (12)$$

By substituting the slip angular velocity in (11) into (12), the relationship between the square of secondary current and thrust is derived as

$$i_{2d}^2 + i_{2q}^2 = \left(\frac{2\tau L_1 F_e}{3\pi L_{meq}\psi_{1d}}\right)^2. \quad (13)$$

Consequently, substituting (11) and (13) into (6), the total loss of LIM will be solved by

$$\begin{aligned} P_{LIM} &= \frac{3}{2}\left(\frac{R_1}{L_1^2} + \frac{k\omega_2^2}{R_c}\right)\psi_{1d}^2 + \frac{2\tau\omega_2 F_e}{\pi R_c}\left(R_1 + \frac{kR_{2eq}L_1^2}{L_{meq}^2}\right) \\ &\quad + \left[R_1\left(1 + \frac{R_{2eq}L_1^2}{R_c L_{meq}^2} + \frac{2\sigma L_1 L_2}{L_{meq}^2}\right)\right. \\ &\quad \left. + \frac{kR_{2eq}L_1^2}{L_{meq}^2}\left(1 + \frac{R_{2eq}L_1^2}{R_c L_{meq}^2}\right)\right]\frac{2\tau^2 F_e^2}{3\pi^2\psi_{1d}^2} \\ &= a_1\psi_{1d}^2 + a_2 + a_3\psi_{1d}^{-2} \end{aligned} \quad (14)$$

where $k = (R_1 + R_c)/R_c$, a_1, a_2, and a_3 are the loss coefficients, which are used to simplify the expression. The optimized variable ψ_{1d} will be analytically attained as below by setting the derivative of P_{LIM} equal to zero, as illustrated by

$$\frac{\partial P_{\mathrm{LIM}}}{\partial \psi_{1d}} = 0 \Rightarrow |\boldsymbol{\psi}_{1opt}| = \psi_{1d opt} = \sqrt[4]{\frac{a_3}{a_1}}. \quad (15)$$

It is worth mentioning that, compared to the secondary flux loss model and optimal flux solution method in [10], the core loss can be more easily presented by primary flux under the condition of primary field orientation. As a result, the proposed loss model has lower order and the optimal flux is easier to solve, which is one of its superiorities.

Fig. 4(a) shows the LIM loss under different primary flux levels at 11 m/s (the adopted parameters are listed in Table I). It can be clearly seen that the LIM loss is a convex function of primary flux, which verifies the feasibility of efficiency optimization by adjusting the flux to an optimal level. Fig. 4(b) depicts the optimal primary flux based on (15) under different speeds and loads. It can be seen from the surface color that as the speed increases, the optimal flux under the same load decreases gradually. This is reasonable due to that reducing the optimal flux will balance the increase in core loss with the increasing speed.

Under light loads, the optimal primary flux decreases rapidly as the load decreases, meaning that the constant flux would lead to high loss. However, the insufficient flux may cause standstill,

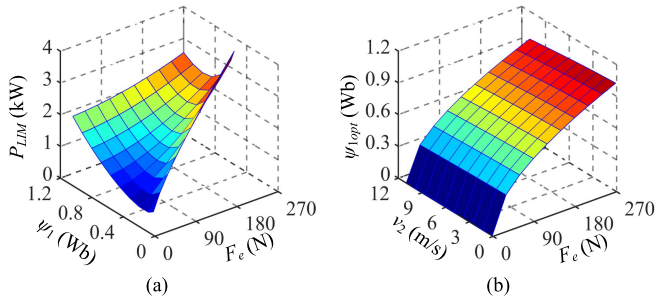

Fig. 4. (a) LIM loss under different primary flux levels at 11 m/s. (b) Optimal primary flux level under different speeds and loads.

TABLE I
MAIN PARAMETERS OF THE LIM

Quantity	Symbol	Value	Unit
Primary length	l_s	1.3087	m
Pole pitch	τ	0.1485	m
Primary resistance	R_1	1.06	Ω
Primary leakage inductance	L_{l1}	9	mH
Magnetizing inductance	L_{m0}	35	mH
Core-loss resistance	R_c	479	Ω
Secondary resistance	R_2	2.4	Ω
Secondary leakage inductance	L_{l2}	3.8	mH
Rated power	P_N	3	kW
Rated speed	v_N	11	m/s
Rated thrust	F_N	270	N

and also causes a large current impact when the load is increased suddenly. To prevent this, the primary flux should be constrained under low-level boundary. Based on (9), the square of d-axis component of primary flux can be derived by

$$\psi_{1d}^2 = \frac{2\tau R_{2eq} L_1^2 F_e}{3\pi L_{meq}^2}\left[\left(\frac{\sigma L_2}{R_{2eq}}\right)^2 \omega_s + \frac{1}{\omega_s}\right] \geq \frac{4\tau\sigma L_1^2 L_2 F_e}{3\pi L_{meq}^2}. \tag{16}$$

The minimum value for primary flux is then determined as

$$|\boldsymbol{\psi}_1| = \psi_{1d} \geq \frac{2L_1}{L_{meq}}\sqrt{\frac{\tau\sigma L_2 F_e}{3\pi}}. \tag{17}$$

To further evaluate the impact of approximation made in (10), the optimal primary flux without approximation is also obtained for comparison. Based on the basic relationship in (1), (3), and (10), the slip angular frequency without approximation can be obtained by solving the quadratic equation, as given by

$$\omega_s = \frac{3\pi R_{2eq} L_{meq}^2 \psi_{1d}^2 - \sqrt{\left(3\pi R_{2eq} L_{meq}^2 \psi_{1d}^2\right)^2 - \left(4\tau\sigma L_1^2 L_2 R_{2eq} F_e\right)^2}}{4\tau(\sigma L_1 L_2)^2 F_e}. \tag{18}$$

The loss can be similarly obtained by using the slip frequency in (18). For a given speed and load, by numerically calculating and comparing the losses under different primary fluxes, the optimal primary flux without approximation can be obtained. Fig. 5 shows the difference between the optimal primary flux with and without approximation. As can be seen, the error

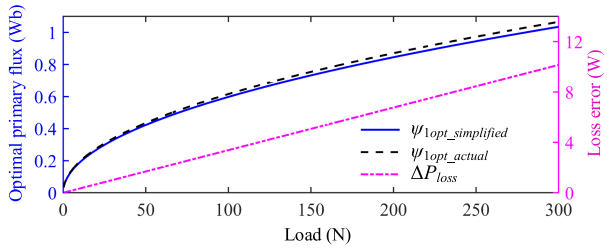

Fig. 5. Difference between the optimal primary flux and LIM loss with and without approximation.

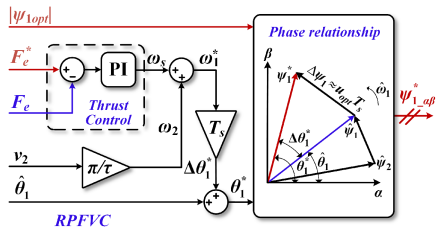

Fig. 6. Block diagram of RPFVC.

in the optimal flux primary with and without approximation becomes larger with the increasing load, and the error under rated load is about 0.03 Wb. It is noticeable that the loss curve is comparatively smooth around the optimal flux point, as shown in Fig. 4(a), so that this flux error has little effect on the loss, only 10 W under heavy loads.

B. Predictive Optimal Primary Flux Control Under Low Switching Frequency

On the basis of the obtained optimal primary flux, minimizing the tracking error of thrust and optimal primary flux is the prior aim to realize efficiency optimization for 3L-NPC inverter-fed LIM drives. Meanwhile, the NPV balance should be considered and the switching frequency should be kept within 500 Hz for the actual operation of linear metro. Finally, high voltage jumps should be avoided. How to effectively deal with the multiple different dimensional objectives and propose a computationally efficient control method with no weighting factors tuning work will be elaborated in the following steps.

1) Control Targets Conversion and Primary Flux Estimation: In this article, the reference flux vector calculator stated in [26] is further extended to the application of LIM drives, named as reference primary flux vector calculator (RPFVC). As shown in Fig. 6, the equivalent reference primary flux vector can be converted from the reference thrust and optimal flux, which is regarded as a new control target. In this way, the reference thrust and loss minimization condition are successfully reflected in the phase angle and magnitude of the reference primary flux vector, respectively. The control target with two different dimensions is no longer needed.

Different from the existing LIM predictive control methods [2], [18], the influence of core-loss resistance will be fully considered in the state estimation and prediction process. Due to the introduction of core-loss resistance and placing it before primary

leakage inductance, the primary current cannot be selected as the state variable as that of the conventional LIM model. In this article, the current through the primary leakage inductance $\boldsymbol{i}_{1m}$ and primary flux ψ_1 are selected as the state variables to derive the prediction model, and the state-space model of LIM in $\alpha\beta$ frame considering the core-loss resistance can be derived as

$$p\boldsymbol{x} = \boldsymbol{A}\boldsymbol{x} + \boldsymbol{B}\boldsymbol{u} \tag{19}$$

where $\boldsymbol{x} = [\boldsymbol{i}_{1m\_\alpha\beta} \ \ \psi_{1\_\alpha\beta}]^{\mathrm{T}}$ are the state variables, $\boldsymbol{u} = \boldsymbol{u}_{1\_\alpha\beta}$ is the primary voltage vector, $\boldsymbol{A} = [-\lambda(R_xL_2+R_2L_1)+j\omega_2 \ \lambda(R_2\text{-}j\omega_2L_2); \ -R_x \ \ 0]$, $\boldsymbol{B} = [\lambda L_2/k \ \ 1/k]^{\mathrm{T}}$, $R_x = R_1/k$, $\lambda = 1/(L_1L_2 - L_{meq}^2)$, and the subscript $\_\alpha\beta$ is used to distinguish the variables from synchronous reference frame. Based on (19), a full-order observer is adopted for primary flux estimation due to its insensitivity to parameter variation, as given by

$$p\hat{\boldsymbol{x}} = \boldsymbol{A}\hat{\boldsymbol{x}} + \boldsymbol{B}\boldsymbol{u}_{opt\_\alpha\beta} + \boldsymbol{G}\left(\boldsymbol{i}_{1m\_\alpha\beta} - \hat{\boldsymbol{i}}_{1m\_\alpha\beta}\right) \tag{20}$$

where $\hat{\boldsymbol{x}} = [\hat{\boldsymbol{i}}_{1m\_\alpha\beta} \quad \hat{\boldsymbol{\psi}}_{1\_\alpha\beta}]^{\mathrm{T}}$ are the estimated states for current and flux, $\boldsymbol{u}_{opt\_\alpha\beta}$ is the optimal VV obtained at (k-1)th instant, and $\boldsymbol{G}$ the feedback gain matrix, which is designed as $\boldsymbol{G} = [2b \ b/(\lambda L_2)]^{\mathrm{T}}$ ($b > 0$) [27]. In (20), the actual current through the primary leakage inductance at kth instant can be calculated with the sampled phase current, as expressed by

$$\boldsymbol{i}_{1m\_\alpha\beta}^{k} = \left[(R_1 + R_c)\boldsymbol{i}_{1\_\alpha\beta}^{k} - \boldsymbol{u}_{opt\_\alpha\beta}\right]/R_c. \tag{21}$$

2) Cost Function Design and Reference VV Calculation: By predicting the control variables one step further, the cost function considering delay compensation can be designed as

$$J = \left\|\boldsymbol{\psi}_{1\_\alpha\beta}^{*} - \boldsymbol{\psi}_{1\_\alpha\beta}^{k+2}\right\|^2 + k_f\left\|\boldsymbol{u}_{1\_\alpha\beta}^{k+1} - \boldsymbol{u}_{opt\_\alpha\beta}\right\|^2 \tag{22}$$

where the first term penalizes the flux and thrust tracking performance, and the second term penalizes the switching effort by the switching positions. The parameter k_f is the penalty factor, which can be used to adjust the switching frequency online. According to (19), the predicted primary flux at (k+2)th instant can be derived by

$$\boldsymbol{\psi}_{1\_\alpha\beta}^{k+2} = \hat{\boldsymbol{\psi}}_{1\_\alpha\beta}^{k+1} + T_s\boldsymbol{u}_{1\_\alpha\beta}^{k+1}/k - R_xT_s\boldsymbol{i}_{1m\_\alpha\beta}^{k+1} \tag{23}$$

where $\hat{\boldsymbol{\psi}}_{1\_\alpha\beta}^{k+1}$ and $\boldsymbol{i}_{1m\_\alpha\beta}^{k+1}$ are predicted for one-step delay based on the second-order Euler discretization of (19), as given by

$$\begin{cases} \boldsymbol{x}_p^{k+1} = (\boldsymbol{I} + \boldsymbol{A}T_s)\boldsymbol{x}^k + \boldsymbol{B}T_s\boldsymbol{u}_{opt\_\alpha\beta} \\ \boldsymbol{x}^{k+1} = \boldsymbol{x}_p^{k+1} + 0.5 \times \boldsymbol{A}T_s(\boldsymbol{x}_p^{k+1} - \boldsymbol{x}^k). \end{cases} \tag{24}$$

By substituting (23) into (22), it obtains

$$\begin{aligned} J = T_s^2\left\|\boldsymbol{u}_{1\_\alpha\beta}^{*} - \boldsymbol{u}_{1\_\alpha\beta}^{k+1}\right\|^2 + k_f\left\|\boldsymbol{u}_{1\_\alpha\beta}^{k+1} - \boldsymbol{u}_{opt\_\alpha\beta}\right\|^2 = T_s^2J' \\ \Rightarrow J' = \left\|\boldsymbol{u}_{1\_\alpha\beta}^{*} - \boldsymbol{u}_{1\_\alpha\beta}^{k+1}\right\|^2 + \lambda_{sw}\left\|\boldsymbol{u}_{1\_\alpha\beta}^{k+1} - \boldsymbol{u}_{opt\_\alpha\beta}\right\|^2 \end{aligned} \tag{25}$$

where $\lambda_{sw} = k_f/T_s^2$. And $\boldsymbol{u}_{1\_\alpha\beta}^{*}$ is the reference VV only considering the flux tracking performance, which can be obtained by letting the predicted flux at (k+2)th instant equal to its reference value, as solved by

$$\boldsymbol{u}_{1\_\alpha\beta}^{*} = k\left(\boldsymbol{\psi}_{1\_\alpha\beta}^{*} - \hat{\boldsymbol{\psi}}_{1\_\alpha\beta}^{k+1}\right)\Big/T_s + R_1\boldsymbol{i}_{1m\_\alpha\beta}^{k+1}. \tag{26}$$

Then, according to the following relationship:

$$\begin{aligned} &m_1\|X - X_1\|^2 + m_2\|X - X_2\|^2 \\ &= (m_1 + m_2)\left\|X - \frac{m_1X_1 + m_2X_2}{m_1 + m_2}\right\|^2 \\ &\quad + \frac{m_1m_2}{m_1 + m_2}\|X_1 - X_2\|^2. \end{aligned} \tag{27}$$

With $m_1 = 1$, $m_2 = \lambda_{sw}$, $X = \boldsymbol{u}_{1\_\alpha\beta}^{k+1}$, $X_1 = \boldsymbol{u}_{1\_\alpha\beta}^{*}$, and $X_2 = \boldsymbol{u}_{opt\cdot\alpha\beta}$, the cost function J' in (25) can be further rearranged as

$$\begin{aligned} J' = (1 + \lambda_{sw})\left\|\boldsymbol{u}_{1\_\alpha\beta}^{k+1} - \frac{\boldsymbol{u}_{1\_\alpha\beta}^{*} + \lambda_{sw}\boldsymbol{u}_{opt\_\alpha\beta}}{1 + \lambda_{sw}}\right\|^2 \\ + \frac{\lambda_{sw}}{1 + \lambda_{sw}}\left\|\boldsymbol{u}_{1\_\alpha\beta}^{*} - \boldsymbol{u}_{opt\_\alpha\beta}\right\|^2. \end{aligned} \tag{28}$$

Since the last term in (28) is a constant value for different evaluated VVs, the cost function in (28) can be further simplified as

$$J_I = \left\|\boldsymbol{u}_{1\_\alpha\beta}^{k+1} - \frac{\boldsymbol{u}_{1\_\alpha\beta}^{*} + \lambda_{sw}\boldsymbol{u}_{opt\_\alpha\beta}}{1 + \lambda_{sw}}\right\|^2 = \left\|\boldsymbol{u}_{1\_\alpha\beta}^{k+1} - \boldsymbol{u}^{*}\right\|^2. \tag{29}$$

It can be seen that when the switching frequency is penalized, the reference VV $\boldsymbol{u}^{*}$ is the synthetic vector of $\boldsymbol{u}_{1\_\alpha\beta}^{*}$ and the last optimal VV $\boldsymbol{u}_{opt\_\alpha\beta}$.

3) Simplified Optimal VV Search Method With Sequential Scheme: Besides the tracking requirement for reference thrust and primary flux, NPV balance is another crucial control goal for 3L-NPC inverter-fed motor drives. In order to realize NPV balance and general requirement for LIM drives, one simplified optimal VV search method with sequential scheme is achieved in two separate steps, as illustrated as follows.

Step I: Calculate the NPV and judge whether the permissible variation limitation ε is exceeded or not. Usually, the fluctuation of the NPV cannot exceed 5% of the dc-link voltage for different voltage levels [28]. And in this article, the limitation ε is predefined as 2.5% of the dc-link voltage. If the NPV is within the permissible limitation, only the tracking performance for thrust and primary flux will be considered. At this time, the evaluation for cost function J_{I} can be solved by the geometric relationship on the output voltage plane.

In order to exclude as many evaluated VVs as possible in advance, the output voltage plane has been divided into six parts with the medium VVs as the dividing line, namely Sectors I–VI, as shown in Fig. 7. Then, a hexagon region is further defined to divide each sector into three regions, namely $R_{1\text{–}3}$, which is formed with the perpendicular bisector of VV lines in the same sector. In this case, the number of evaluated VVs can be reduced from 27 to a maximum of 3 by determining the region of reference VV directly. For example, $\boldsymbol{u}_{13}$ (ONN) and $\boldsymbol{u}_{14}$ (POO) will be evaluated when the reference VV is located in R_2 of Sector I. Besides, $\boldsymbol{u}_{25}$ (OOO) will be selected as the only zero VV when the reference VV is located in R_1. Both $\boldsymbol{u}_{26}$ (NNN) and

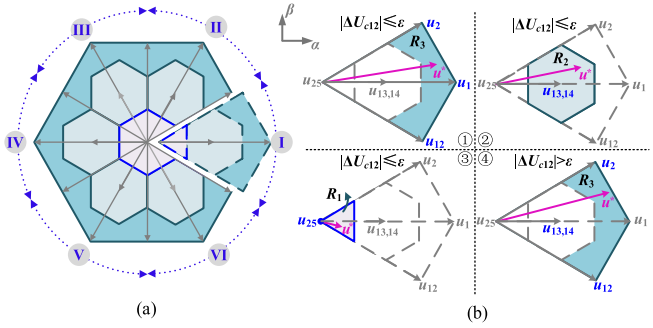

Fig. 7. Regions division and evaluated VVs. (a) Sectors and Regions division. (b) Evaluated VVs in different cases.

$\boldsymbol{u}_{27}$ (PPP) are ruled out, the reasons are summarized as follows: 1) These three VVs have the same effect on the flux control and NPV balance, 2) $\boldsymbol{u}_{25}$ (OOO) has the smallest common-mode voltage, and 3) $\boldsymbol{u}_{25}$ (OOO) can realize smooth switching with all other VVs. In order to facilitate the judgment, the reference VV in other sectors can be transformed to Sector I first, and then the above analysis can be used analogously.

Step II: If the NPV exceeds the permissible limitation, the NPV balance should also be considered. At this time, besides the control objective given in (29), one more objective is formulated by the following cost function, as expressed by:

$$J_{\mathrm{II}} = \left\| \Delta U_{c12}^{k+2} \right\|^2 \tag{30}$$

where ΔU_{c12}^{k+2} is calculated based on (5) with the consideration of delay compensation. It can be concluded from (5) that only small VVs and medium VVs can affect the NPV balance. Hence, the reference VV $\boldsymbol{u}^*$ is calculated first, and then the small and medium VVs in the same sector as $\boldsymbol{u}^*$ are evaluated for J_{II}. With this sequential optimization scheme, the weighting factor for NPV can be avoided, and the reference VV independent of NPV can be used to simplify the optimal VV selection.

Furthermore, to avoid a high voltage jump or shoot-through, switching state transition between P and N is forbidden in 3L-NPC inverter. Thus, a switching state hard constraint S_m must be included in the cost function J_{I} and J_{II}, which is given by

$$S_m = \begin{cases} 0 & \text{if } x \in \{a,b,c\}, \forall x : |S_x^{k+1} - S_x^k| \leqslant 1 \\ \infty & \text{otherwise} \end{cases}. \tag{31}$$

Since S_m just outputs two dimensionless values, its introduction does not affect the reference VV calculation, as given in (29).

As can be seen in (29), there still exists one weighting factor λ_{sw} in the proposed PFC-EOS that needs to be adjusted to achieve the desired switching frequency. To further avoid cumbersome tuning of λ_{sw} based on trial and error, it is online adapted according to the following equation:

$$\lambda_{sw}^{k+1} = \lambda_{sw}^{k} + \Delta\lambda_{sw} \tag{32}$$

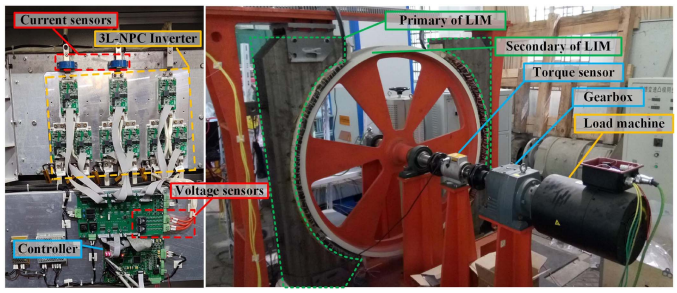

Fig. 8. Experimental setup for a 3L-NPC inverter-fed LIM drives.

where $\Delta\lambda_{sw}$ is the variation step of λ_{sw}. To balance the settling time and accuracy, the variation step $\Delta\lambda_{sw}$ is designed as

$$\Delta\lambda_{sw} = \begin{cases} 0.002T_s \times (f_{sw} - f_{sw}^*) & \text{if } |f_{sw} - f_{sw}^*| > 75 \\ 0.05T_s \times sgn(f_{sw} - f_{sw}^*) & \text{otherwise} \end{cases} \tag{33}$$

where f_{sw}^* is the desired switching frequency, and $sgn(\bullet)$ the sign function. f_{sw} is the average switching frequency, which is calculated online by counting the total switching transitions N of 12 IGBTs over a duration T, i.e., $f_{sw} = N/(T \times 12)$. In (33), the step is related to its tracking error instead of using a const value. When the tracking error is large, a large variation step related to the error is used to rapidly reduce the tracking error. When the tracking error is less than 75 Hz, the step will be constant, thus reducing the fluctuation near the desired switching frequency. Meanwhile, it is worth mentioning that the regulation mechanism, as described in (32) and (33), can be regarded as a closed-loop system, with which the switching frequency will eventually reach the desired value. Hence, the design of coefficients in variation step does not affect the final value of switching frequency, and thus, does not have much impact on the steady-state and dynamic drive performance.

IV. Experimental Results and Analysis

In order to validate the effectiveness of the proposed method, experiments are carried out on one prototyped 3 kW LIM platform driven by a 3L-NPC inverter, as shown in Fig. 8. Main parameters used in the validation are given in Table I. Considering the testing space, two coupled arc induction machines with large enough diameter (1.25 m) are used to simulate the properties of an actual LIM [29]. The sampling frequency for predictive control is set to 12 kHz, and the dc-link voltage is 450 V. The control unit used in the inverter is DSP TMS320F28335. Besides the proposed method, the following three methods are applied to the platform for comparisons: 1) constant excitation commonly used in urban transit under the framework of predictive flux control (PFC-CE), 2) predictive flux control-based MTPA in [18] (PFC-MTPA), and 3) the efficiency optimization strategy under the framework of FOC in [10] (FOC-EOS).

A. Validation of Primary Flux-Based Loss Model

The effectiveness of the proposed primary flux-based loss model for LIM is first investigated. A HIOKI PW6001-16 power analyzer is used for measuring the input power to the LIM, and

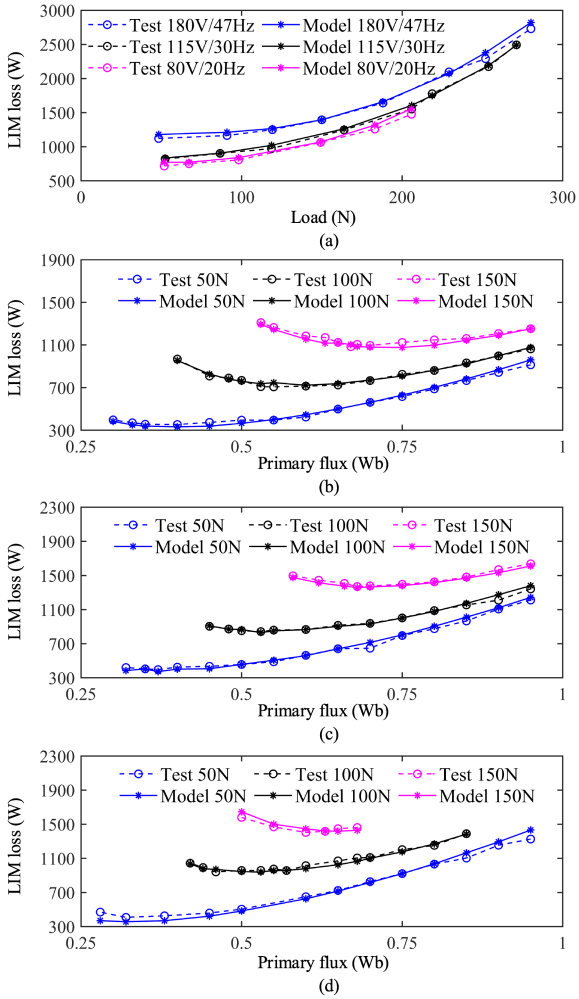

Fig. 9. Comparisons between the measured and calculated losses for LIM under various loads and primary fluxes. (a) Variable voltage and variable frequency. (b) 5 m/s. (c) 11 m/s. (d) 13 m/s.

the output power is calculated from the measured speed and shaft torque (measured with a ZHK-D torque sensor), so that the LIM loss can be determined. By recording the speed, load thrust and primary flux of LIM, the calculated loss under different operating conditions can be obtained based on (14). Fig. 9 shows the comparisons between the measured and calculated losses, in which the LIM is driven to operate under various loads and primary fluxes. It can be found that most of the calculated losses based on the loss model can match the measured counterparts well, with a maximum relative error around 5%. The flux value corresponding to the lowest point of each curve is the optimal primary flux under a certain speed and load. In order to better illustrate the change of the optimal flux with the speed, the optimal flux corresponding to different speeds are obtained according to the results shown in Fig. 9, as listed in Table II. It can be seen that the optimal flux corresponding to the same load gradually decreases with the increasing speed, which is consistent with the theoretical analysis.

However, for some points under light loads, especially under high speeds and light loads, there are some differences between

TABLE II
OPTIMAL PRIMARY FLUX UNDER DIFFERENT CONDITIONS (UNIT: WB)

Working condition	50 N	100 N	150 N
5 m/s	0.37	0.55	0.70
11 m/s	0.35	0.53	0.66
13 m/s	0.34	0.51	0.64

loss model and experiments. The reasons for the difference under light loads mainly come from the following two aspects. First, the prototyped LIM platform faces many external interferences and resistances during running, especially the windage resistance and viscous friction, which are not considered in the loss model. Under the condition of high speeds, light loads, and low flux level, the machine loss is small, so that the impact of windage resistance and viscous friction will be amplified. As a result, the measured loss is larger than that calculated by the loss model. Second, the core loss in this article ignores the nonlinear influence, such as variable frequency power supply, end-effect magnetic field distortion, and rich spatial harmonics. These nonlinear influence factor makes the actual core loss variation law much more complex. Under high speeds and light loads, the proportion of core loss increases, and the modeling error of core loss leads to a certain deviation between the calculated and the measured value. Although such aspects lead to deviations at some points under light loads, it can be indicated from most of the well-matched points that the proposed loss model is available to reflect the motor loss.

B. Steady-State and Dynamic Performances

Fig. 10 shows experimental results when adaptive adjusting λ_{sw} online to achieve low switching frequency operation. During the test, the switching frequency is updated about every 0.07 s. In Fig. 10(a), when the desired switching frequency is changed from 800 Hz to 200 Hz, weighting factor λ_{sw} can be adaptively increased to a value around 0.2 to limit the switching actions. Fig. 10(b) depicts the steady-state waveform of line-to-line voltage corresponding to the switching frequencies of 800 Hz and 200 Hz in Fig. 10(a), showing that the switching actions are suppressed significantly after the switching frequency is decreased. Fig. 10(c) shows the response of average switching frequency and weighting factor λ_{sw} when the speed steps from 4 m/s to 11 m/s. It can be seen that the average switching frequency deviates from its reference value temporarily during the dynamic process. After the transient process, the average switching frequency can be kept around 350 Hz under a new weighting factor. The test confirms that with the online adjusting of λ_{sw} based on (32) and (33), the average switching frequency of the PFC-EOS can be flexibly regulated with strong stability.

The dynamic performances of LIM drives based on the proposed method are shown in Fig. 11. Fig. 11(a) presents the starting and braking process to the rated speed, in which the primary flux can be adjusted to an optimal value according to the system condition. In order to reduce overshoot and improve the comfort of passengers in the actual linear metro, the I gain in the speed PI controller is usually set as a small value due to large

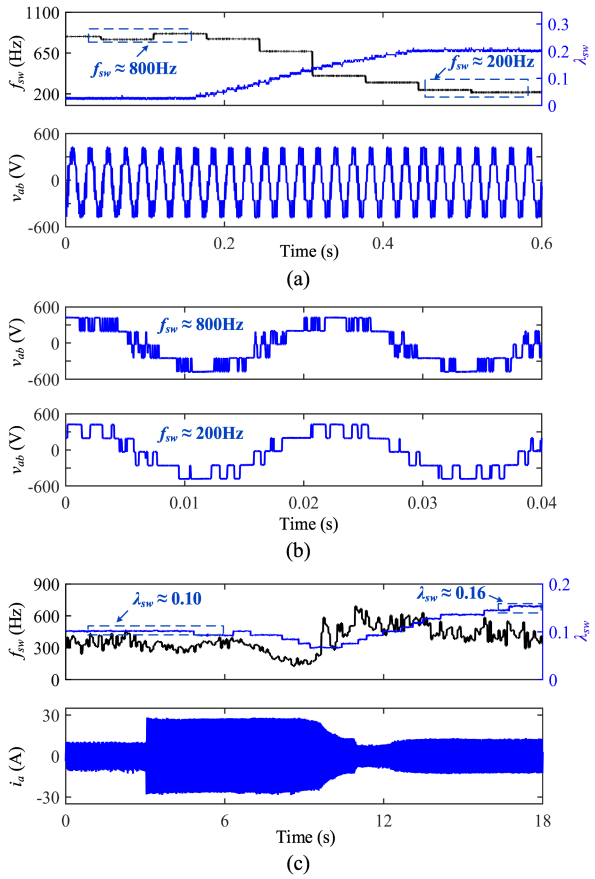

Fig. 10. Experimental results of adaptive adjusting λ_{sw} online to achieve low switching frequency operation. (a) Response under switching frequency step change. (b) Steady-state waveform of line-to-line voltage under different switching frequencies. (c) Response under speed step change.

inertia of the studied LIM. Therefore, when the speed approaches the reference value, the speed PI controller will exit saturation in advance, and the thrust will be reduced from the maximum value. The response to the external load disturbance is depicted in Fig. 11(b). The reference speed is given as rated speed while the load thrust is increased from 50 N to 150 N and then returns to 50 N. The electromagnetic thrust increases quickly to balance the load and the speed recovers its original value after a speed drop. Under low switching frequency and large modulation ratios, the thrust fluctuations will inevitably increase. However, our application, linear metro, is a large inertia system, in which the speed is not sensitive to thrust fluctuations. Hence, a certain range of thrust fluctuations is acceptable. Moreover, in order to verify the effect of sequential optimization scheme on NPV balance, the performance under different permissible variation limitations is tested as shown in Fig. 11(c). After the limitation ε is changed from 150 V to 10 V, the NPV can be well suppressed within 10 V, and the current and thrust performance are also obviously improved.

Fig. 12 shows the steady-state performance for FOC-EOS and PFC-EOS at 8 m/s and 200 N. As can be seen in Fig. 12(a), the current THD for the proposed PFC-EOS increases slowly with the switching frequencies between 800 and 350 Hz, while it increases quickly along with the decrease of the switching frequency for the FOC-EOS. Specifically, as shown in Fig. 12(b) and (c), the current THD can be reduced from 11.16% to 7.19% when using PFC-EOS instead of FOC-EOS at 350 Hz. Reducing current distortion will be helpful to reduce the core loss and harmonic loss in the LIM, thereby further increasing efficiency and reducing heating. In addition, low current distortion usually means low thrust fluctuations and noise, thus reducing the possibility of mechanical transmission problems in linear metro.

The step responses of electromagnetic thrust are compared for different methods. As seen from Fig. 13, the settling times are close for the three predictive control methods. By adaptively adjusting the weighting factor λ_{sw}, the PFC-EOS can be easily implemented with a high sampling frequency while keeping a low switching frequency. However, the FOC-EOS shows a much slower settling process. On the one hand, predictive flux control takes thrust and primary flux as the control quantity, and does not need the modulation, leading to a faster response than FOC. On the other hand, the PWM generation mechanism between FOC-EOS and PFC-based methods is different. The reduction of switching frequency in FOC-EOS is generally achieved by extending the sampling period. For a switching frequency of 350 Hz, the FOC scheme is allowed to update the PWM and control the currents approximately every 1429 μs. At such a long control period, the dynamic response becomes slow and the disturbance rejection also becomes poor. This can be seen as a limitation of FOC-EOS, which is difficult to operate at a high sampling frequency with a low switching frequency. Moreover, it should be noted that the update frequency of the state variables in FOC-EOS is very low due to a long control period, resulting in outputting the same value for a long time, as shown by the black line in Fig. 13. As a result, the thrust waveform of FOC-EOS in Fig. 13 can only reflect the dynamic response, many instantaneous fluctuations cannot be shown. The above results validate that the proposed PFC-EOS can successfully achieve a better steady-state and dynamic performance under low switching frequency than FOC-EOS.

C. *Efficiency Analysis*

Since PFC-CE, PFC-MTPA, and PFC-EOS have the same control scheme, these methods can be switched directly. The changes in input power, phase current, and primary flux during the switching process are shown in Fig. 14. The LIM operates with const excitation (0.8 Wb) under 5 m/s at first, and then switches to PFC-MTPA and PFC-EOS under the same working condition. To better illustrate the differences between each method, comparisons for phase current and synchronization frequency are shown in Fig. 15. PFC-MTPA takes the minimum primary current as the target to determine the reference flux, so that it has the minimum primary current among three methods, i.e., the minimum primary copper loss, as shown in Fig. 15(a). By significantly reducing the primary copper loss under light loads, the loss of PFC-MTPA is less than PFC-CE.

However, it should be noted that PFC-MTPA increases the synchronization frequency while minimizing the primary current, as can be seen in Fig. 15(b). Under the same speed, the

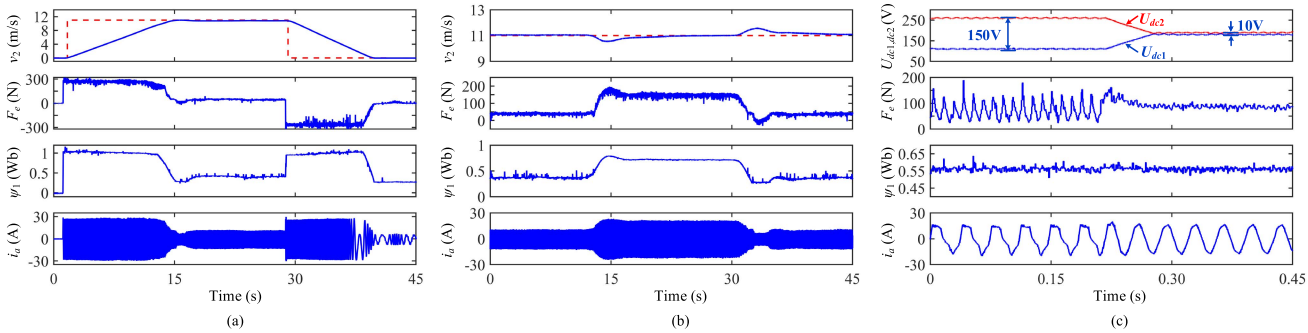

Fig. 11. Experimental results of the dynamic response for PFC-EOS. (a) Starting and breaking process to the rated speed 11 m/s. (b) External load disturbance under the rated speed 11 m/s. (c) NPV balance under the proposed sequential optimization scheme.

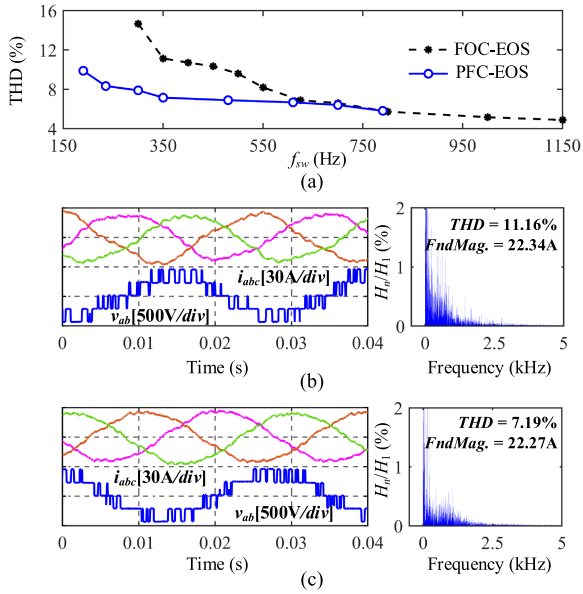

Fig. 12. Experimental results of steady-state performance for FOC-EOS and PFC-EOS at 8 m/s and 200 N. (a) Current THD under different switching frequencies. (b) Performance for FOC-EOS under switching frequency of 350 Hz. (c) Performance for PFC-EOS under switching frequency of 350 Hz.

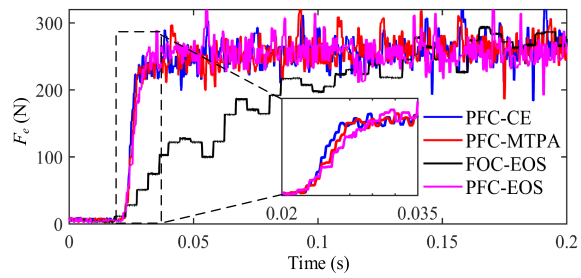

Fig. 13. Experimental results of the transient performance for different methods under switching frequency of 350 Hz.

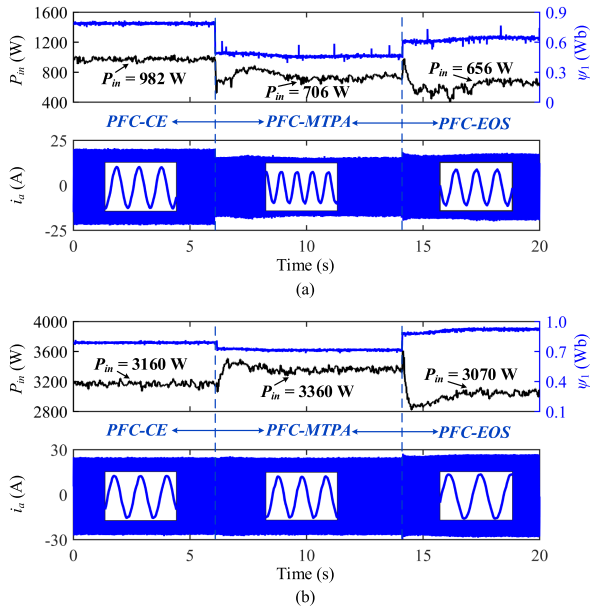

Fig. 14. Experimental results of the dynamic switching between different methods. (a) 5 m/s and 50 N. (b) 5 m/s and 250 N.

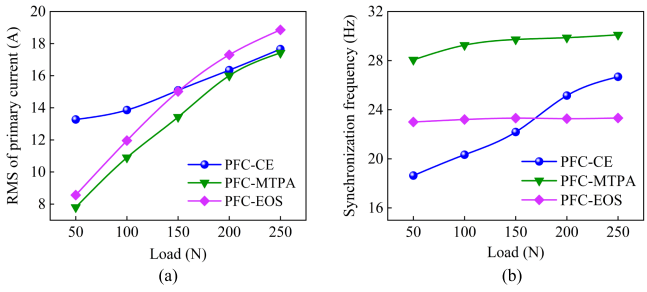

Fig. 15. Rms of phase current and synchronization frequency for different methods under 5 m/s. (a) Rms of phase current. (b) Synchronization frequency.

increase of synchronization frequency leads to the increase in secondary copper loss and core loss. Therefore, although PFC-MTPA minimizes the primary copper loss, it cannot guarantee the minimum total loss. On the contrary, the proposed PFC-EOS directly solves the optimal flux with the minimum total loss. As a result, although the primary current is increased compared to PFC-MTPA, the total loss can be fully considered and minimized under different working conditions.

More comprehensive comparisons on loss and efficiency for different methods are shown in Figs. 16 and 17. Compared to

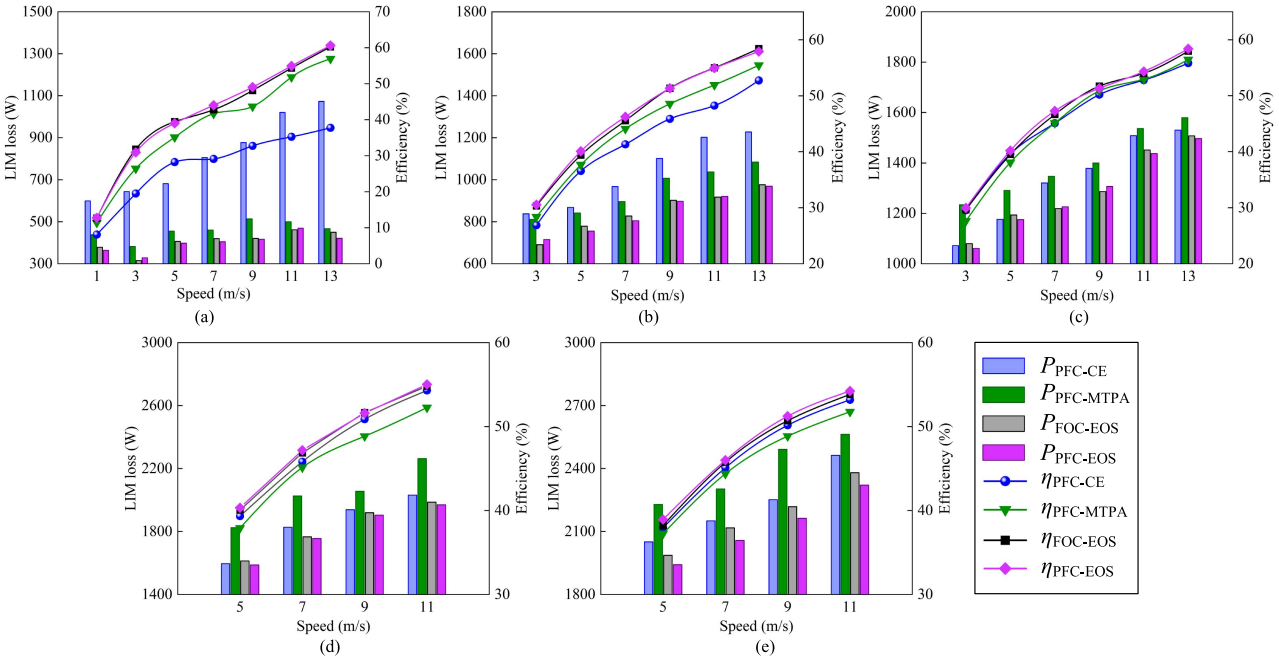

Fig. 16. Comparisons on LIM loss and efficiency for different methods under various speeds and loads. (a) 50 N. (b) 100 N. (c) 150 N. (d) 200 N. (e) 250 N.

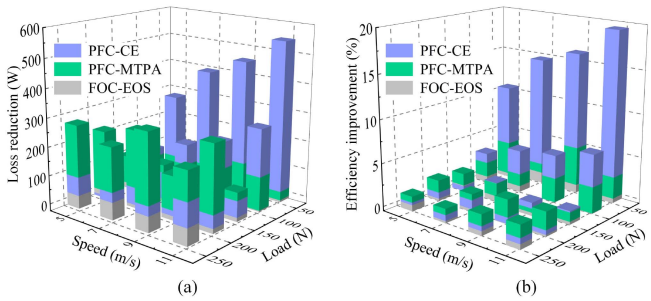

Fig. 17. Loss reduction and efficiency improvement compared to the existing methods. (a) Loss reduction. (b) Efficiency improvement.

existing methods, the reasons of loss reduction and efficiency improvement for PFC-EOS are summarized as follows.

1) A constant flux reference can only guarantee high efficiency near certain working conditions, usually near the rated load. Thereof, the efficiency for PFC-CE is low under light loads due to excessive copper loss, as shown in Fig. 16(a) and (b). PFC-EOS can significantly improve the LIM efficiency at light loads by reducing the copper loss compared to PFC-CE. Although the efficiency improvement of PFC-EOS is relatively minor under heavy loads, it tends to increase as the load increases by making the flux higher than the rated value, as shown in Fig. 16(d) and (e).
2) With the increasing load, the slip and the proportion of secondary copper loss increases rapidly. PFC-MTPA only minimizes the primary copper loss by minimizing the primary current. Correspondingly, the results in Fig. 16(d) and (e) show that PFC-MTPA has a poor effect on improving efficiency when the load is larger than 150 N. It can be concluded that in most cases, PFC-MTPA is not the best strategy to improve efficiency especially for machines, which work with large slips, such as LIM.
3) Compared to the FOC-EOS, the advantage of PFC-EOS is mainly reflected in the reduction of harmonic loss at low switching frequency. However, due to the small power of the prototype, the impact of harmonic loss is not fully reflected under light loads. Hence, it can be seen from Fig. 14(a)–(c) that the efficiency of the two methods is basically close when ignoring the measurement error. Under the load of 250 N, the loss of PFC-EOS can be further reduced by about 60–80 W, as shown in Fig. 17, resulting in higher efficiency.

D. Parameter Sensitivity Evaluation

Parameters play an important role in optimal flux calculation and manipulation, and thus, affect the final results, i.e., efficiency and control performance. Hence, parameter sensitivity on the proposed method is analyzed here. By intentionally detuning the parameters from their nominal values, the control performance of PFC-EOS under 11 m/s and 150 N is shown in Fig. 18. From the experimental results, it can be seen that the parameter mismatches mainly affect the primary flux, while the thrust shows some fluctuations after the parameters change. However, the system can still run stably after the parameter variation, which means the control performance is robust to parameter variation.

Since the mismatched parameters deteriorate the optimal operating point, Fig. 19 further validates the LIM efficiency reduction ratio for different parameter mismatches under various loads at 11 m/s. Among the mismatched parameters, the magnetizing inductance has the most significant impact, which causes

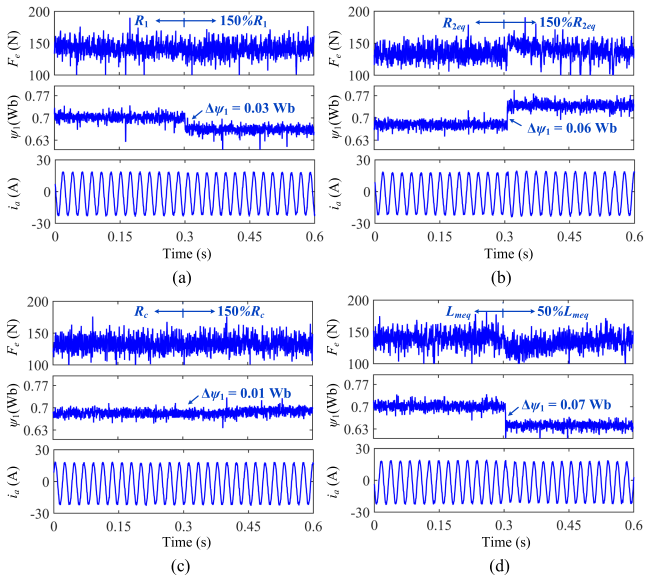

Fig. 18. Experimental results of parameter sensitivity valuation for the proposed PFC-EOS under 11 m/s and 150 N. (a) Primary resistance mismatch. (b) Secondary resistance mismatch. (c) Core-loss resistance mismatch. (d) Magnetizing inductance mismatch.

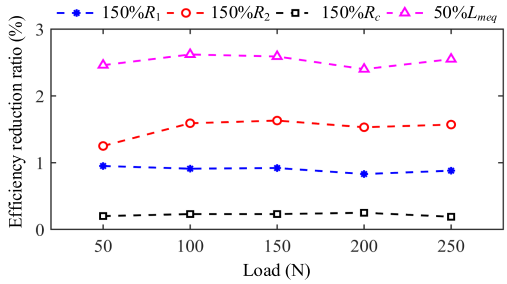

Fig. 19. LIM efficiency reduction ratio for different parameter mismatches under various loads at 11 m/s.

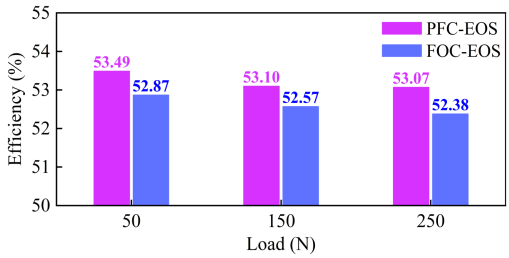

Fig. 20. Efficiency comparison for PFC-EOS and FOC-EOS under mismatched magnetizing inductance at 11 m/s.

the LIM efficiency to reduce by 2.5% under different loads. For other parameters, the reduction ratio in efficiency is less than 2%. Fig. 20 shows the efficiency comparison for PFC-EOS and FOC-EOS under the same mismatched magnetizing inductance, where the magnetizing inductance is changed to 50% of its original value. Like PFC-EOS, FOC-EOS also has the problem of efficiency decline under parameters mismatch. It can be seen from Fig. 20 that the efficiency improvement advantage of

TABLE III
QUANTITATIVE PERFORMANCE COMPARISONS FOR DIFFERENT METHODS UNDER THE SWITCHING FREQUENCY OF 350 HZ

Index		PFC-CE	PFC-MTPA	FOC-EOS	**PFC-EOS**
Current THD		7.14%	7.27%	11.16%	**7.19%**
Thrust step response		6.7 ms	8.3 ms	98.2 ms	**9.1 ms**
η	11 m/s, 50 N	35.24%	51.83%	54.33%	**54.84%**
	11 m/s, 150 N	52.78%	52.93%	53.99%	**54.52%**
	11 m/s, 250 N	53.19%	51.76%	53.83%	**54.43%**
Sampling period		83.33 μs	83.33 μs	1429 μs	**83.33 μs**
Execution time		30.0 μs	32.1 μs	40.1 μs	**35.8 μs**

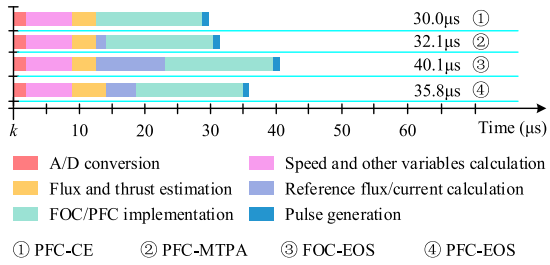

Fig. 21. Execution time comparison of different methods.

the proposed method still exists. Being affected by parameters mismatch is an inherent problem of model-based EOSs. Aiming at robustness enhancement is a striving direction for future work, and the research must also be carried out based on the results of this article.

E. Overall Performance Comparisons

Finally, overall performance comparisons between the proposed method and the existing methods are summarized in Table III, in which the average switching frequency of different methods is controlled at 350 Hz. Compared with the PFC-CE, PFC-MTPA, and FOC-EOS, the LIM efficiency with PFC-EOS can be increased by 19.60%, 3.01%, and 0.51% under 11 m/s and 50 N, which is the cruising condition in linear metro. The corresponding efficiency improvement under 11 m/s and 250 N are 1.24%, 2.67%, and 0.60%, accompanied by loss reductions of 142 W, 242 W, and 60 W, respectively.

Fig. 21 further details the execution time in the form of a bar chart, which is measured in real-time implementation. With the proposed sector division and simplified VV search method, the execution time of predictive control can be less than that of FOC. Moreover, the primary flux-based loss model has lower order, so that optimal flux can be calculated in half the time of the secondary-flux based loss model. Compared with FOC-EOS, the proposed PFC-EOS not only realizes the efficiency optimization for LIM, but also guarantees the steady-state and dynamic performance under low switching frequency. Therefore, PFC-EOS is more suitable for actual application of linear metro, and it is also convenient to further integrate other advanced methods, such as parameter identification and sensorless control.

V. Conclusion

This article proposes a PFC-EOS for 3L-NPC inverter-fed LIM drive system to improve the LIM efficiency under low switching frequency. First, one novel primary flux-based loss model is established, where the loss is expressed as a convex function of primary flux. Based on this model, the optimal primary flux for minimum machine loss can be derived analytically in a simple form. Then, a computationally efficient predictive flux control with sequential optimization scheme is developed for optimal flux manipulation. In the proposed PFC-EOS, core-loss resistance is further considered in the prediction and flux estimation to improve accuracy. Multiple additional control demands are effectively tackled and tedious tuning work for weight factors is avoided. Finally, extensive experimental comparisons are performed among the proposed method and the existing methods, confirming that better efficiency improvement can be achieved under low switching frequency. Taking the cruising condition in linear metro as an example, the LIM efficiency with PFC-EOS can be increased by 19.60%, 3.01%, and 0.51% compared with the PFC-CE, PFC-MTPA, and FOC-EOS, respectively.

For further development of the proposed scheme, the hybrid efficiency optimization strategy combined with the search method will be fully studied, which can further enhance the robustness of the proposed method and improve the convergence speed of the traditional search method.

References

[1] G. Lv, D. Zeng, and T. Zhou, "An advanced equivalent circuit model for linear induction motors," *IEEE Trans. Ind. Electron.*, vol. 65, no. 9, pp. 7495–7503, Sep. 2018.

[2] Y. Tang, W. Xu, D. Dong, Y. Liu, and M. M. Ismail, "Low-complexity multistep sequential model predictive current control for three-level inverter-fed linear induction machines," *IEEE Trans. Ind. Electron.*, vol. 70, no. 6, pp. 5537–5548, Jun. 2023.

[3] I. Boldea, L. N. Tutelea, W. Xu, and M. Pucci, "Linear electric machines, drives, and MAGLEVs: An overview," *IEEE Trans. Ind. Electron.*, vol. 65, no. 9, pp. 7504–7515, Sep. 2018.

[4] M. Habibullah, D. D. Lu, D. Xiao, J. E. Fletcher, and M. F. Rahman, "Predictive torque control of induction motor sensorless drive fed by a 3L-NPC inverter," *IEEE Trans. Ind. Inform.*, vol. 13, no. 1, pp. 60–70, Feb. 2017.

[5] X. Long, *Theory and Magnetic Design Method of Linear Inductionmotor*. Beijing, China: Science, 2006, pp. 69–74.

[6] Q. Lu, Y. Li, Y. Ye, and Z. Q. Zhu, "Investigation of forces in linear induction motor under different slip frequency for low-speed," *IEEE Trans. Energy Convers.*, vol. 28, no. 1, pp. 145–153, Mar. 2013.

[7] Z. Qu, M. Ranta, M. Hinkkanen, and J. Luomi, "Loss-minimizing flux level control of induction motor drives," *IEEE Trans. Ind Appl.*, vol. 48, no. 3, pp. 952–961, May/Jun. 2012.

[8] W. Xu, R. Islam, and M. Pucci, *Advanced Linear Machines Drive Systems*. Berlin, Germany: Springer-Verlag, 2019.

[9] A. Accetta, M. C. Di Piazza, M. Luna, and M. Pucci, "Electrical losses minimization of linear induction motors considering the dynamic end-effects," *IEEE Trans. Ind. Appl.*, vol. 55, no. 2, pp. 1561–1573, Mar./Apr. 2019.

[10] D. Hu, W. Xu, R. Dian, Y. Liu, and J. Zhu, "Loss minimization control of linear induction motor drive for linear metros," *IEEE Trans. Ind. Electron.*, vol. 65, no. 9, pp. 6870–6880, Sep. 2018.

[11] X. Xiao et al., "Improved loss minimization control based on time-harmonic equivalent circuit for linear induction motors adopted to linear metro," *IEEE Trans. Veh. Technol.*, vol. 72, no. 7, pp. 8601–8612, Jul. 2023.

[12] J. Holtz, "Advanced PWM and predictive control–an overview," *IEEE Trans. Ind. Electron.*, vol. 63, no. 6, pp. 3837–3844, Jun. 2016.

[13] A. Andersson and T. Thiringer, "Assessment of an improved finite control set model predictive current controller for automotive propulsion applications," *IEEE Trans. Ind. Electron.*, vol. 67, no. 1, pp. 91–100, Jan. 2020.

[14] M. Habibullah, D. D.-C. Lu, D. Xiao, I. Osman, and M. F. Rahman, "Selected prediction vectors based FS-PTC for 3L-NPC inverter fed motor drives," *IEEE Trans. Ind. Appl.*, vol. 53, no. 4, pp. 3588–3597, Jul./Aug. 2017.

[15] C. Xia, T. Liu, T. Shi, and Z. Song, "A simplified finite-control-set model-predictive control for power converters," *IEEE Trans. Ind. Inform.*, vol. 10, no. 2, pp. 991–1002, May 2014.

[16] Z. Zhang, C. M. Hackl, and R. Kennel, "Computationally efficient DMPC for three-level NPC back-to-back converters in wind turbine systems with PMSG," *IEEE Trans. Power Electron.*, vol. 32, no. 10, pp. 8018–8034, Oct. 2017.

[17] Y. Zhang, Y. Bai, H. Yang, and B. Zhang, "Low switching frequency model predictive control of three-level inverter-fed IM drives with speed-sensorless and field-weakening operations," *IEEE Trans. Ind. Electron.*, vol. 66, no. 6, pp. 4262–4272, Jun. 2019.

[18] W. Xu, Y. Tang, D. Dong, X. Xiao, E. E. M. Rashad, and A. K. Junejo, "Optimal reference primary flux based model predictive control of linear induction machine with MTPA and field-weakening operations for urban transit," *IEEE Trans. Ind. Appl.*, vol. 58, no. 4, pp. 4708–4721, Jul./Aug. 2022.

[19] M. Preindl and S. Bolognani, "Model predictive direct torque control with finite control set for PMSM drive systems, part 1: Maximum torque per ampere operation," *IEEE Trans. Ind. Inform.*, vol. 9, no. 4, pp. 1912–1921, Nov. 2013.

[20] S. R. Eftekhari, S. A. Davari, P. Naderi, C. Garcia, and J. Rodriguez, "Robust loss minimization for predictive direct torque and flux control of an induction motor with electrical circuit model," *IEEE Trans. Power Electron.*, vol. 35, no. 5, pp. 5417–5426, May 2020.

[21] Y. Wang, T. Ito, and R. D. Lorenz, "Loss manipulation capabilities of deadbeat direct torque and flux control induction machine drives," *IEEE Trans. Ind. Appl.*, vol. 51, no. 6, pp. 4554–4566, Nov./Dec. 2015.

[22] W. Xie, X. Wang, F. Wang, W. Xu, R. Kennel, and D. Gerling, "Dynamic loss minimization of finite control set-model predictive torque control for electric drive system," *IEEE Trans. Power Electron.*, vol. 31, no. 1, pp. 849–860, Jan. 2016.

[23] X. Li, K. Lu, Y. Zhao, D. Chen, P. Yi, and W. Hua, "Incorporating harmonic-analysis-based loss minimization into MPTC for efficiency improvement of FCFMPM motor," *IEEE Trans. Ind. Electron.*, vol. 70, no. 7, pp. 6540–6550, Jul. 2023.

[24] Y. Tang, W. Xu, J. Ge, Y. Shangguan, Y. Liu, and K. Liao, "Efficiency optimization based predictive thrust and flux control for three-level inverter-fed linear induction machine adapted to urban transit," in *Proc. IEEE Int. Conf. Predictive Control Elect. Drives Power Electron.*, 2023, pp. 1–6.

[25] W. Xu et al., "Equivalent circuits for single-sided linear induction motors," *IEEE Trans. Ind. Appl.*, vol. 46, no. 6, pp. 2410–2423, Nov./Dec. 2010.

[26] D. Xiao, K. S. Alam, I. Osman, M. P. Akter, S. M. S. I. Shakib, and M. F. Rahman, "Low complexity model predictive flux control for three-level neutral-point clamped inverter-fed induction motor drives without weighting factor," *IEEE Trans. Ind. Appl.*, vol. 56, no. 6, pp. 6496–6506, Nov./Dec. 2020.

[27] Y. Zhang and H. Yang, "Model-predictive flux control of induction motor drives with switching instant optimization," *IEEE Trans. Energy Convers.*, vol. 30, no. 3, pp. 1113–1122, Sep. 2015.

[28] J. Holtz and N. Oikonomou, "Neutral point potential balancing algorithm at low modulation index for three-level inverter medium- voltage drives," *IEEE Trans. Ind. Appl.*, vol. 43, no. 3, pp. 761–768, May/Jun. 2007.

[29] A. Majumdar and T. K. Bhattacharya, "Comparison of force developed in a linear induction machine and an equivalent arc linear induction machine at zero velocity," in *Proc. IEEE Int. Conf. Power Electron., Drives Energy Syst.*, 2018, pp. 1–5.

Yirong Tang (Graduate Student Member, IEEE) received the B.E. degree in 2020 from Huazhong University of Science and Technology, Wuhan, China, where he is currently working toward the Ph.D. degree with the State Key Laboratory of Advanced Electromagnetic Technology, both in electrical engineering.

His research interests include advanced control methods for linear induction machines, permanent magnet synchronous machines, and drives.

Wei Xu (Fellow, IEEE) received the double B.E. and M.E. degrees from Tianjin University, Tianjin, China, in 2002 and 2005, respectively, and the Ph.D. from the Institute of Electrical Engineering, Chinese Academy of Sciences (IEECAS), Beijing, China, in 2008, all in electrical engineering.

From 2008 to 2012, he was a Postdoctoral Fellow with the University of Technology Sydney, Vice Chancellor Research Fellow with Royal Melbourne Institute of Technology, Japan Science Promotion Society Invitation Fellow with Meiji University, respectively. From 2013 to 2023, he was one Professor with Huazhong University of Science and Technology, China. Since 2024, he has been one Professor with IEECAS. His research interest includes design and control for linear machines and drives.

Dr. Xu is Fellow of the Institute of Engineering and Technology. He is the General Chair for 2021 International Symposium on Linear Drives for Industry Applications and 2023 IEEE International Conference on Predictive Control of Electrical Drives and Power Electronics. He was an Associate Editor for over ten peer-review IEEE journals, including IEEE TRANSACTIONS ON INDUSTRIAL ELECTRONICS and IEEE TRANSACTIONS ON POWER ELECTRONICS.

Jian Ge (Member, IEEE) was born in Heilongjiang, China, in 1994. He received the B.E., M.E., and Ph.D. degrees in electrical engineering from Huazhong University of Science and Technology, Wuhan, China, in 2016, 2019, and 2022, respectively.

He is currently a Postdoctoral Researcher in electrical engineering with Huazhong University of Science and Technology. His research interests include induction machines, linear machines, and brushless doubly-fed machines.

Yongdao Shangguan received the B.E. degree in marine electronic and electrical engineering from Dalian Maritime University, Dalian, China, in 2021. He is currently working toward the Ph.D. degree in electrical engineering with the School of Electrical Engineering, Huazhong University of Science and Technology, Wuhan, China.

His research interest includes design and control of linear machines.

Yaohua Li (Member, IEEE) was born in Henan, China, in 1966. He received the Ph.D. degree in power electronics and power drives from Tsinghua University, Beijing, China, in 1994.

From 1995 to 1997, he was a Postdoctoral Research Fellow with the Institute of Electrical Machines, Technical University of Berlin, Berlin, Germany. In 1997, he was with the Institute of Electrical Engineering, Chinese Academy of Sciences, Beijing, China, where he is currently a Professor and the Director. His current research interests include the analysis and control of electrical machines and power electronics.

Wenye Yuan received the B.E. degree in electrical engineering from Northwestern Polytechnical University, Xi'an, China, in 2006.

He has been with Zhuzhou CRRC Times Electric Company, Ltd., since 2006. He was engaged in product development of linear machines and drive systems.